Applied Catalysis B: Environmental 312 (2022) 121386

Contents lists available at ScienceDirect

Applied Catalysis B: Environmental

journal homepage: www.elsevier.com/locate/apcatb

A dual-functional supramolecular assembly for enhanced photocatalytic hydrogen evolution

Lin Qin, Ruijie Wang, Xing Xin, Mo Zhang, Tianfu Liu, Hongjin Lv *, Guo-Yu Yang *

MOE Key Laboratory of Cluster Science, Beijing Key Laboratory of Photoelectroic/Electrophotonic Conversion Materials, School of Chemistry and Chemical Engineering, Beijing Institute of Technology, Beijing 102488, PR China

ARTICLE INFO

Keywords:
Supramolecular assembly
Ir-based chromophore
Polyoxometalate catalyst
Visible-light-driven H_2 evolution
Photocatalysis

ABSTRACT

The construction of multifunctional supramolecular assembly is a central research interest in solar-driven water splitting to hydrogen. We here report the successful preparation of a dual-functional supramolecular assembly *via* facile electrostatic integration of a positively-charged Ir-based chromophore and a negatively-charged nickel-substituted polyoxometalate catalyst. The resulting dual-functional supramolecule can form ordered vesicle-like assemblies and work efficiently as both light-absorber and catalyst for hydrogen production under visible light irradiation. Under minimally optimized conditions, a catalytic hydrogen production turnover number of over 4000 was achieved after 96-hour irradiation, which is 17 times to that of discrete components under otherwise identical conditions. Destruction of such ordered vesicle-like assemblies will lead to a remarkable decrease of photocatalytic hydrogen production activity. Mechanistic studies further revealed the presence of both oxidative and reductive quenching processes during photocatalysis and also confirmed that the formation of ordered supramolecule is beneficial for effective electron transfer between chromophore and catalyst.

1. Introduction

The over-consumption and depletion of fossil fuels have been causing serious energy shortage and environmental problems in especially recent few decades [1,2]. One of the promising approaches to solve these problems is to explore cost-effective, clean, and sustainable energy alternatives [3–7]. Direct conversion from inexhaustible sunlight to storable and renewable chemical fuels through water splitting is one of the ideal strategies for the development of a sustainable hydrogen economy [8–13]. In a typical three-component hydrogen-evolving system, it usually contains photosensitizers (PS) to absorb sunlight, multi-electron-transfer catalysts to catalyze hydrogen production, and sacrificial reagents to scavenge photogenerated holes, respectively. However, the presence of three separated components could lead to a complicated system, in which the effective hydrogen generation process will be affected by many factors [6]. To better control the electron transfer process and enhance the catalytic efficiency, supramolecular photocatalysts that integrate light-absorbers and catalysts together has been designed and established in recent years [14–16]. For example, Ru- or Ir-based light-absorbing units have been connected with Pd-, Pt- or Co-based water-reduction catalysts for hydrogen production [14–20]. The shortened charge-transfer distance and decreased ineffective collisions between photosensitizers and catalysts of conventional discrete molecular systems have promoted electron transfer efficiency, leading to highly efficient hydrogen evolution activity [6].

With respect to the design of hydrogen-evolving catalysts, transition-metal-substituted polyoxometalates (POMs) have been employed as an emerging type of multi-electron transfer catalysts for photocatalytic hydrogen production in recent years, owing to their tunable molecular structures and rich photochemical properties [4,21–31]. After years of development, various metal-substituted POMs (e.g. Mn, Ni, Co, and Cu, etc.) have achieved catalytic H_2 generation activity in the presence of visible-light-absorbing photosensitizers and sacrificial reagents [23,24,27,32–41]. To integrate POMs and photosensitizers into one molecule, POMs could be modified with organic ligands to attach Ir- or Ru-based complexes [42–47]. The reported covalently-linked PS-POM supramolecules exhibited improved charge separation and electron transfer in hydrogen evolution reaction [43,44]. However, the formation of such type PS-POM supramolecules linked by covalent bonds demanded exhausting synthetic work and was only applicable for a few types of POMs [43,45]. Given the high negatively-charged nature of POM polyoxoanions, their counter cations are readily to be replaced through

* Corresponding authors.
E-mail addresses: hlv@bit.edu.cn (H. Lv), ygy@bit.edu.cn (G.-Y. Yang).

https://doi.org/10.1016/j.apcatb.2022.121386
Received 18 February 2022; Received in revised form 29 March 2022; Accepted 6 April 2022
Available online 8 April 2022

simple cation-exchange approach [48]. The facile exchange of counter cations could influence the structural assemblies and material performance, giving rise to polyoxometalate-based self-assemblies with various functions [48–51]. For example, tuning the length and steric hindrance of alkyl ammoniums cations could afford core-shell shaped or layer-by layer arranged architectures based on polyoxometalates [49,52,53]. Nevertheless, reports on electrostatic POM supramolecules formed by light-absorbing chromophores and POMs are limited [53–57]. Replacing one cation of $PW_{12}O_{40}^{3-}$ by $Ru(bpy)_3^{2+}$ led to formation of **$[Ru(bpy)_3]$ $[KPW_{12}O_{40}]$** hybrid, which was probed the presence of strong electrostatic interaction from crystallographic data [53]. Assembled from four positively charged Chlorin and one negatively charged $[\alpha\text{-}SiMo_{12}O_{40}]^{4-}$, supramolecular Chlorin-POM complex showed enhanced activity in photodynamic therapy [54]. Electrostatically formed PS-POM complexes have been immobilized on the surface of TiO_2-modified photoanodes and applied for photoelectrocatalysis [55,56]. Despite those known literature reports, the research of using such electrostatic interaction induced PS-POM supramolecules for solar-driven hydrogen production remains largely unexplored.

Herein, we report the successful construction of a dual-functional supramolecular assembly *via* facile electrostatic integration of a positively-charged Ir-based chromophore and a negatively-charged nickel-substituted polyoxometalate catalyst. The resulting dual-functional supramolecule can form ordered vesicle-like assemblies and work efficiently as both light-absorber and catalyst for hydrogen production under visible light irradiation. Various spectroscopic characterization results strongly confirmed that the successful formation of ordered supramolecular vesicle-like assemblies in reaction solution is essential for efficient photocatalytic hydrogen production. This work provides new possibilities for the development of supramolecular photocatalytic hydrogen production systems, such facile cation-exchange approach could also be extended to construct other dual-functional photosensitizer-catalyst supramolecules for other interesting catalytic applications.

2. Experimental

2.1. Materials and Instrumentation

Na_2HPO_4, $Na_2WO_4.2\ H_2O$, $Ni(OOCCH_3)_2.4\ H_2O$, $K(OOCCH_3)$, acetic acid, 2-methoxyethanol, 4,4′-dinonyl-2,2′-bipyridine, 3-(2-Benzothiazolyl)− 7-(diethylamino)coumarin (coumarin 6), and Iridium (III) chloride trihydrate were purchased from TCI and used as received. **Na_6K_4-Ni_4P_2** POM was prepared according to reported procedure and further confirmed by single crystal X-ray diffraction as well as Fourier Transform Infrared (FT-IR) spectrum [32]. **$(C_9Ir)_6$-Ni_4P_2** supramolecule was obtained by exchange of counter cations with **C_9Ir^+** unit from **Na_6K_4-Ni_4P_2** POM. All solvents and other reagents were used as received.

Proton Nuclear Magnetic Resonance (^{1}H NMR) spectra were recorded on a Bruker Ascend 400 M (Avance IIIHD 400 MHz) fourier transform NMR spectometer with chemical shifts (δ, ppm) relative to tetramethylsilane (Me_4Si). High resolution electrospray ionization mass spectra (ESI-MS) were obtained on AGILENT Q-TOF 6520 mass spectrometer. Infrared spectra were acquired on a Bruker TENSOR II FT-IR spectrometer by preparing dry solid samples mixing with KBr pellets. UV–vis absorption spectra were recorded on the UV 2600 uv–vis Spectrophotometer and all emission spectra were performed on the EDINBURGH INSTRUMENTS Spectrofluorometer FS5. Errors for λ values (± 1 nm) were estimated. Emission lifetime were measured with a EPL-450 PICOSECOND PULSED DIODE laser system (pulse output 450 nm). Inductively coupled plasma (ICP) mass spectrometry was carried out by X Series 2 ICP-MS. X-ray photoelectron spectroscopy (XPS) data was performed by using PHI 5000 VersaProbe III Scanning XPS Microprobe. Surface morphology and element analysis of samples were obtained from field emission scanning electron microscopy (SEM) JSM-7500 F with a built-in EDS system. Transmission electron microscopy (TEM) images were performed on a JEM-2100 field emission microscope.

2.2. Preparation

2.2.1. Synthetic procedure for $Na_6K_4[Ni_4(H_2O)_2(PW_9O_{34})_2]\cdot 32\ H_2O$ (**Na_6K_4-Ni_4P_2**) [32]

Na_2HPO_4 (1.57 g, 11 mmol) and $Na_2WO_4.2\ H_2O$ (33 g, 100 mmol) was dissolved in H_2O (100 mL), then using concentrated acetic acid to adjust the pH of above solution to 7.0. Subsequently, an aqueous solution (50 mL) of $Ni(OOCCH_3)_2.4\ H_2O$ (5.5 g, 22 mmol) was slowly added. The affording solution was refluxed for 2.5 h and then filtered hot. By adding 4 g of $K(OOCCH_3)$ to the filtrate, the solution was left for vaporing at room temperature. After one day, small yellow green crystals were obtained and collected as the pure products (yield =18.9 g, 62%).

2.2.2. Synthetic procedure for **C_9Ir-Cl**

Firstly, a 2-methoxyethanol/water (3:1 v/v, 50 mL) solution of iridium (III) chloride (0.9 g, 2.56 mmol, 1.0 eq.) and coumarin 6 (1.98 g, 5.64 mmol, 2.2 eq.) was heated at 120 °C for 48 h under Ar atmosphere. After cooled to room temperature, the resulting precipitate was filtered off, washed with H_2O and EtOH, affording Ir(III) μ-chloro-bridged dimer as orange products. Secondly, Ir(III) μ-chloro-bridged dimer complex (400 mg, 0.22 mmol, 1.0 eq.) and 4,4′-dinonyl-2,2′-bipyridine (196 mg, 0.48 mmol, 2.2 eq.) were added to degassed 2-methoxyethanol solution (10 mL). Then the solution was heated at 120 °C for overnight. After removing solvent, the resulting crude product was further purified by silica gel column chromatography using dichloromethane/MeOH (v/v = 1/0–200/1) as the eluent, affording the pure product as orange solids. Yield: 66%. ^{1}H NMR (400 MHz, $CDCl_3$, 298 K): δ9.72 (s, 2 H), 8.24 (d, 2 H, J = 4.0 Hz), 7.80 (d, 2 H, J = 8.0 Hz), 7.33 (d, 2 H, J = 4.0 Hz), 7.23 (m, 2 H, overlap by solvent peak), 6.87 (t, 2 H, J = 8.0 Hz), 6.37 (d, 2 H, J = 4.0 Hz), 6.06 (d, 2 H, J = 12.0 Hz), 5.86 (dd, 2 H, J = 4.0, 4.0 Hz), 5.81 (d, 2 H, J = 8.0 Hz), 3.28 (m, 8 H), 3.10 (m, 2 H), 2.92 (m, 2 H), 1.71 (b, 4 H), 1.25 (d, 24 H, J = 8.0 Hz), 1.09 (t, 12 H, J = 8.0 Hz), 0.87 (t, 6 H, J = 8.0 Hz); HRMS (ESI-MS): Calcd for $[C_{68}H_{78}IrN_6O_4S_2]^+$ ($[M\text{-}Cl]^+$): m/z 1299.516. Found: m/z 1299.536.

2.2.3. Synthetic procedure for $(C_9Ir)_6K_4[Ni_4(H_2O)_2(PW_9O_{34})_2]$ [**$(C_9Ir)_6$-Ni_4P_2**] supramolecule

C_9Ir-Cl complex (40 mg, 11 eq) was dissolved in acetone solution (2.5 mL), resulting in a clear and orange solution. Meanwhile, **Na_6K_4-Ni_4P_2** (15 mg, 1 eq) was dissolved in water (2.0 mL), giving rise to a clear and light green solution. Then, the former acetone solution was added dropwise to the latter aqueous solution, affording large amount of orange precipitates. The mixture was further stirred for 2 days at room temperature in the absence of light. After that, the solids were then filtered off, washed with H_2O and ethanol. The pure product was obtained as orange solids. Elemental analyses confirmed the presence of six **C_9Ir^+** and four K^+ cations in the final supramolecule, which was denoted as **$(C_9Ir)_6$-Ni_4P_2** for simplicity. Yield: 50%. ^{1}H NMR (400 MHz, d^6-DMSO, 298 K): δ 8.62 (d, 2 H, J = 8.0 Hz), 8.55 (s, 2 H), 8.11 (d, 2 H, J = 8.0 Hz), 7.70 (d, 2 H, J = 4.0 Hz), 7.27 (t, 2 H, J = 8.0, 8.0 Hz), 6.89 (t, 2 H, J = 8.0, 8.0 Hz), 6.46 (s, 2 H), 6.03 (s, 4 H), 5.79 (d, 2 H, J = 8.0 Hz), 3.32 (overlap by solvent peak, 8 H), 2.79 (t, 4 H, J = 8.0, 4.0 Hz), 1.63 (br, 4 H), 1.19 (br, 24 H), 0.96 (t, 12 H, J = 8.0, 4.0 Hz), 0.80 (br, 6 H).

2.3. The photocatalytic hydrogen production experiments

Photocatalytic hydrogen production was carried out in DMF/toluene (v/v = 3/1) solution by employing **$(C_9Ir)_6$-Ni_4P_2** supramolecule (40 μM) as both light absorbing chromophore and catalyst, H_2O (2 M) as proton source and TEOA (0.25 M) as sacrificial reagent. Xe lamp (λ > 400 nm, 300 W, Beijing Perfectlight Technology Co., Ltd; PLS-SXE300D) was utilized as the irradiation source. The resulting solution was deaerated

with Ar/CH_4 gas for 25 mins before illumination. All turnover numbers (TONs) were calculated with respect to the amount of **Ni_4P_2** catalyst in the supramolecule. Analysis of H_2 was carried out by using a Thermo GC7900 model gas chromatograph equipped with thermal conductivity detector (TCD) and a 5 Å molecular sieve capillary column. Apparent quantum yield (AQY) is calculated using the hydrogen yield produced in the first 2 h (when hydrogen production rate is linear during this period) [58,59], the detailed calculation procedure is described in the Supporting Information.

3. Results and discussion

3.1. Syntheses and characterization

The 4,4′-dinonyl-2,2′-bipyridine ligand with long alkyl chains was designed and used for the synthesis of C_9Ir-Cl complex (Figs. S1 and S2) with the expectation for ordered self-assembly behaviors. The formation of **$(C_9Ir)_6$-Ni_4P_2** supramolecule (Fig. S3) was achieved *via* facile cation-anion exchange of **Na_6K_4-Ni_4P_2** POM (Fig. S4) and C_9Ir-Cl chromophore. As determined by inductively coupled plasma-atomic emission spectrometry (ICP-AES), the presence of Ni, P, W, Ir, K elements was confirmed in the supramolecule structure. Moreover, the molar ratio of Ir and Ni metals in obtained $(C_9Ir)_6$-Ni_4P_2 supramolecule is 1.522, indicating that the six cations of **Na_6K_4-Ni_4P_2** were replaced by Ir-based **C_9Ir^+** unit, leading to a complete formula of $(C_9Ir)_6K_4[Ni_4(H_2O)_2(PW_9O_{34})_2]$. As reported in literatures, large POMs molecules with high negative charges could easily form vesicles in solution [48,49]. With respect to polyoxoanion of **$[Ni_4P_2]^{10-}$** and steric hindrance of **C_9Ir^+**, we expected that the **$(C_9Ir)_6$-Ni_4P_2** supramolecule could exhibit a vesicle-like assembly in solution where each **Ni_4P_2** polyoxoanion in the

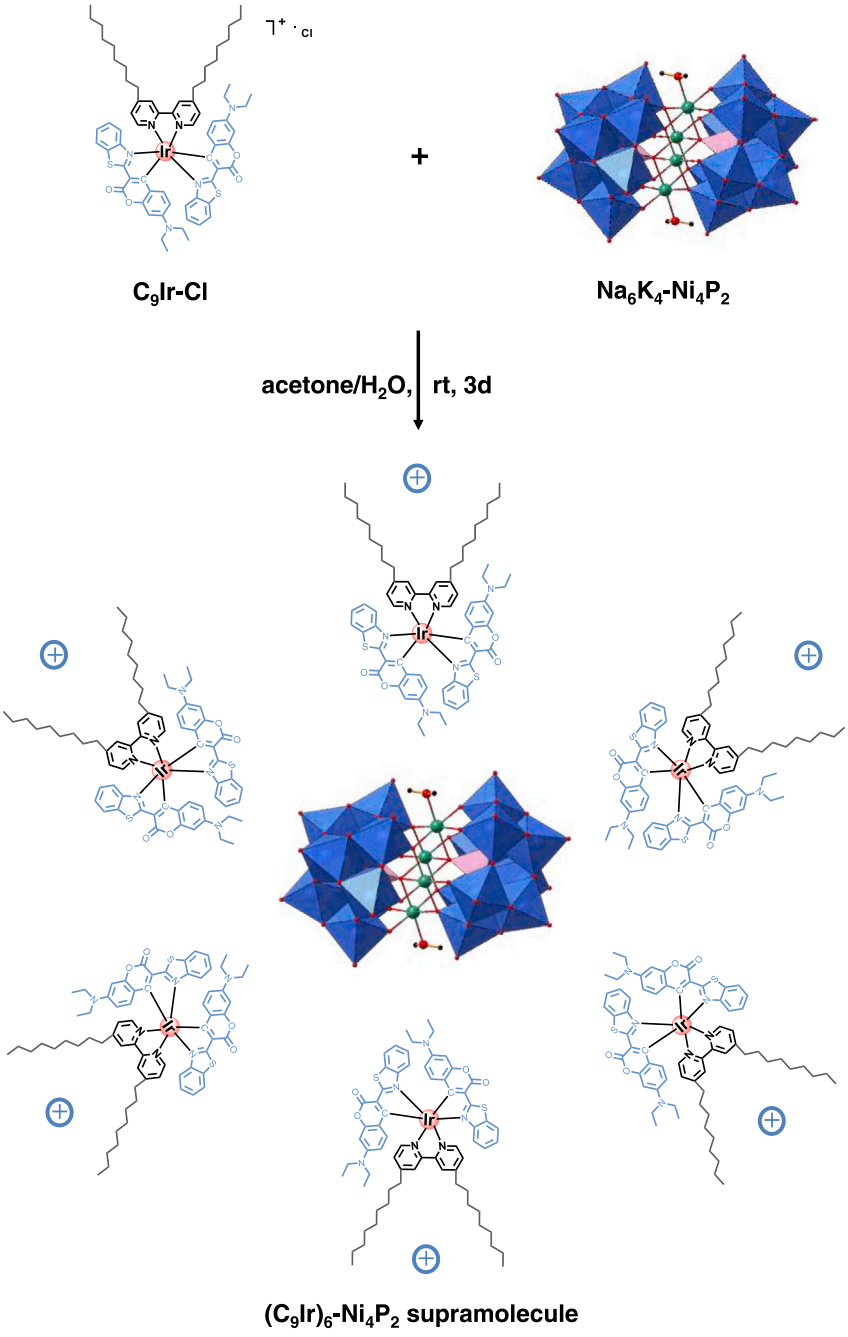

Fig. 1. The schematic illustration of **$(C_9Ir)_6$-Ni_4P_2** supramolecular assembly. Note: the four K^+ cations were omitted for simplicity.

center was surrounded by six C_9Ir^+ cations outside, the schematic illustration of the structure is depicted in Fig. 1, detailed experimental evidence will be discussed in the following sections.

3.2. Characterization of $(C_9Ir)_6$-Ni_4P_2 supramolecule

A series of techniques were employed to rationalize the successful formation of $(C_9Ir)_6$-Ni_4P_2 supramolecule solid sample. As shown in Fig. 2a, Scanning Electron Microscope (SEM) and the corresponding elemental mapping images proved the homogeneous presence of Ir, Ni and P elements. Elemental analyses (Fig. S5) from Energy Dispersive Spectrometer (EDS) confirmed the atomic percentage of 0.94, 0.67, and 0.26 for Ir, Ni, and P, respectively, corresponding to an atomic ratio of 1.4 and 2.6 for Ir/Ni and Ni/P, respectively, which is in good agreement with the composition of $(C_9Ir)_6$-Ni_4P_2 supramolecule. The FT-IR spectrum (Fig. 2b) of $(C_9Ir)_6$-Ni_4P_2 supramolecule shows the characteristic

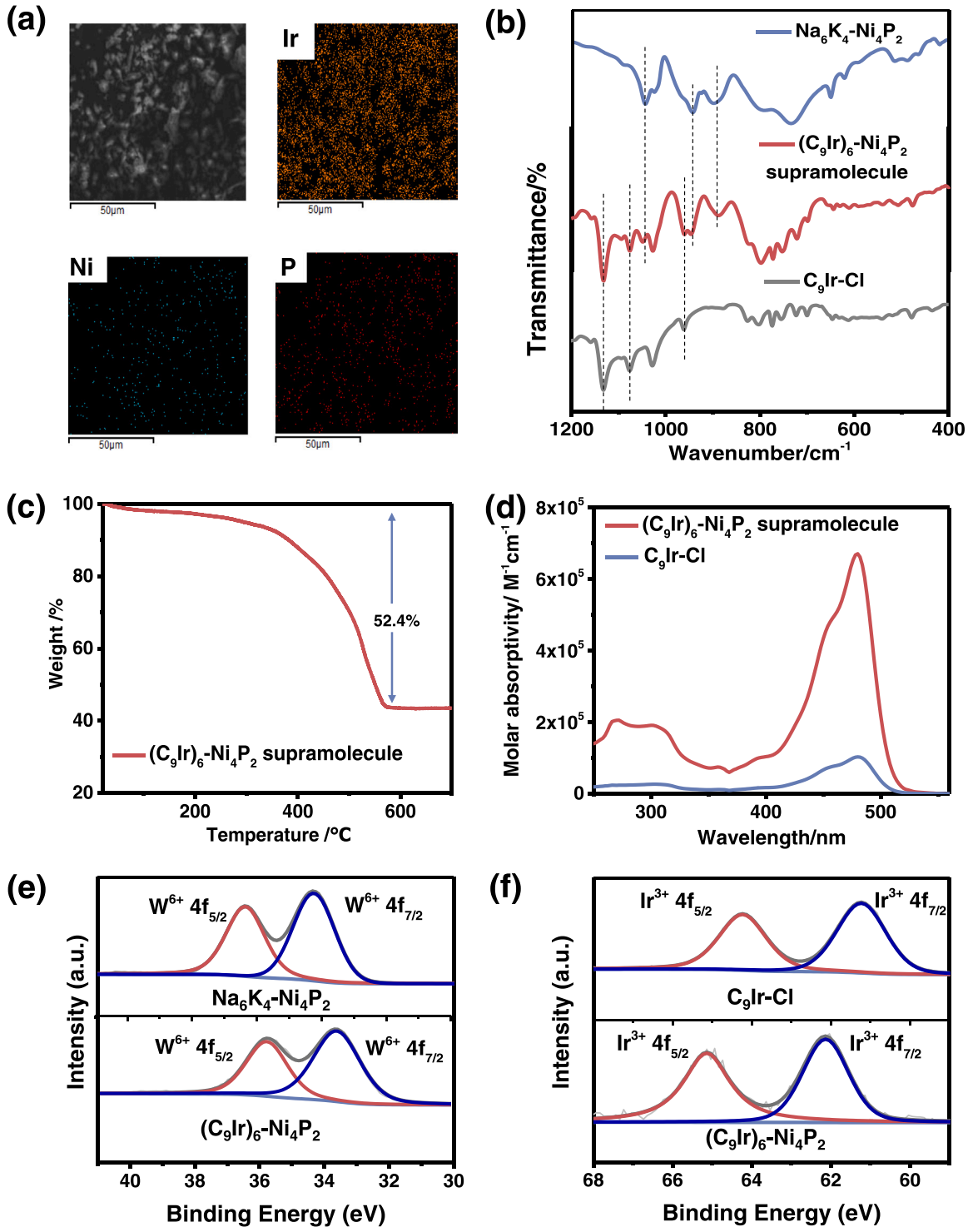

Fig. 2. (a) The corresponding elemental mapping images of $(C_9Ir)_6$-Ni_4P_2; (b) The FT-IR spectra of Na_6K_4-Ni_4P_2, C_9Ir-Cl and $(C_9Ir)_6$-Ni_4P_2; (c) The TGA analysis of $(C_9Ir)_6$-Ni_4P_2 supramolecule. The calculated weight loss percentage of 52.4% corresponding to organic part of six Ir-based complex, respectively; (d) The UV–vis spectra of C_9Ir-Cl and $(C_9Ir)_6$-Ni_4P_2; High resolution XPS spectra of (e) W 4 f, and (f) Ir 4 f signals before and after formation of $(C_9Ir)_6$-Ni_4P_2 supramolecule.

absorption peaks of both **Ni_4P_2** (typical W−O and P − O vibrational bands in 500–1100 cm^{-1}) and Ir-based units, indicating that the exchange of counter cations by **C_9Ir^+** does not change the molecular geometry of **Ni_4P_2** polyoxoanion. In addition, thermogravimetric (TGA) analysis (Fig. 2c) of **$(C_9Ir)_6$-Ni_4P_2** supramolecule displays a sharp weight loss of 52.4% from 200 to 580 ℃, corresponding to the loss of six **C_9Ir^+** cations. As shown in UV-Vis spectra (Fig. 2d), **$(C_9Ir)_6$-Ni_4P_2** supramolecule displays intense absorption bands from 400 nm to 550 nm in DMF solution, which is similar with that of **C_9Ir-Cl**. X-ray photoelectron spectroscopy (XPS) technique was further employed to determine the presence and chemical oxidation states of Ni (Fig. S6), W (Fig. 2e), and Ir (Fig. 2f) elements in both **Ni_4P_2** POM only and **$(C_9Ir)_6$-Ni_4P_2** supramolecule. The specific binding energies confirmed the oxidation states of Ni, W, and Ir elements as + 2, + 6, and + 3, respectively. It is worth mentioning that after formation of **$(C_9Ir)_6$-Ni_4P_2** supramolecule the binding energy of W 4 f exhibits a negative shift by 0.86 eV (Fig. 2e), indicating the shift of electron density from **C_9Ir** units to **Ni_4P_2** clusters due to the strong electronic interaction between them. In the meanwhile, the electron density around **C_9Ir** decreases as displayed by the positive shift (0.91 eV) of Ir 4 f binding energy (Fig. 2f). Such strong electronic interaction was further substantiated by both steady-state and time-resolved solid-state emission studies. As expected, both the emission intensity and the decay lifetimes (Fig. S7 and Table S1) exhibits remarkable decrease with the formation of **$(C_9Ir)_6$-Ni_4P_2** supramolecule, further indicating the effective charge transfer between **Ni_4P_2** POM and **C_9Ir** complex. Moreover, the obvious blue-shift observed in emission spectra of **$(C_9Ir)_6$-Ni_4P_2** supramolecule comparing to that of **C_9Ir-Cl** to is also indicative of strong electrostatic interaction between cationic **C_9Ir^+** and **Ni_4P_2** polyoxoanion [60].

3.3. *Visible-light-driven hydrogen evolution*

Photocatalytic hydrogen production of **$(C_9Ir)_6$-Ni_4P_2** supramolecule was performed in deaerated DMF/toluene (v/v = 3/1) solution with TEOA as sacrificial reagent and H_2O as proton source. The **$(C_9Ir)_6$-Ni_4P_2** supramolecule function as both photosensitizer (**C_9Ir** as the light absorber) and catalyst (**Ni_4P_2** as the catalytic center) in photocatalytic system. With respect to the intense absorption of **$(C_9Ir)_6$-Ni_4P_2** supramolecule in visible light region, Xe lamp (λ > 400 nm, 300 W, Beijing Perfectlight Technology Co., Ltd; PLS-SXE300D) was employed as the irradiation light source. All turnover numbers (TONs) were calculated by dividing the amount of produced H_2 gas to that of **$(C_9Ir)_6$-Ni_4P_2** supramolecule. Upon exposed to strong visible light, the **$(C_9Ir)_6$-Ni_4P_2** catalytic systems achieved efficient hydrogen generation in 10 h with a linear increase trend (Fig. 3). During photocatalysis, the empty 5d orbitals in the W centers of the lacunary **PW_9** ligand of **Ni_4P_2** catalyst exhibit outstanding reversible multi-electron-storing ability, thereby working as the electron-storage sponge for subsequent catalysis. In the meanwhile, the transition metal Ni centers could work as the catalytic active sites for proton reduction to hydrogen as reported by previous works [36,38]. To evaluate the effect of each component, control experiments on varying the concentration of TEOA and **$(C_9Ir)_6$-Ni_4P_2** supramolecule were carried out, respectively. As shown in Fig. 3a and b, the absence of either component resulted in no generation of hydrogen, revealing the indispensable role of **$(C_9Ir)_6$-Ni_4P_2** supramolecule and TEOA to realize efficient water-splitting into hydrogen. Moreover, at constant 20 μM **$(C_9Ir)_6$-Ni_4P_2** supramolecule in the photocatalytic solution, varying the concentration of TEOA from 0.15 M to 0.5 M yield an increasement of hydrogen release from 90 μmol (TON ~748) to 133 μmol (TON ~1105) (Fig. 3a). Adjusting the concentration of

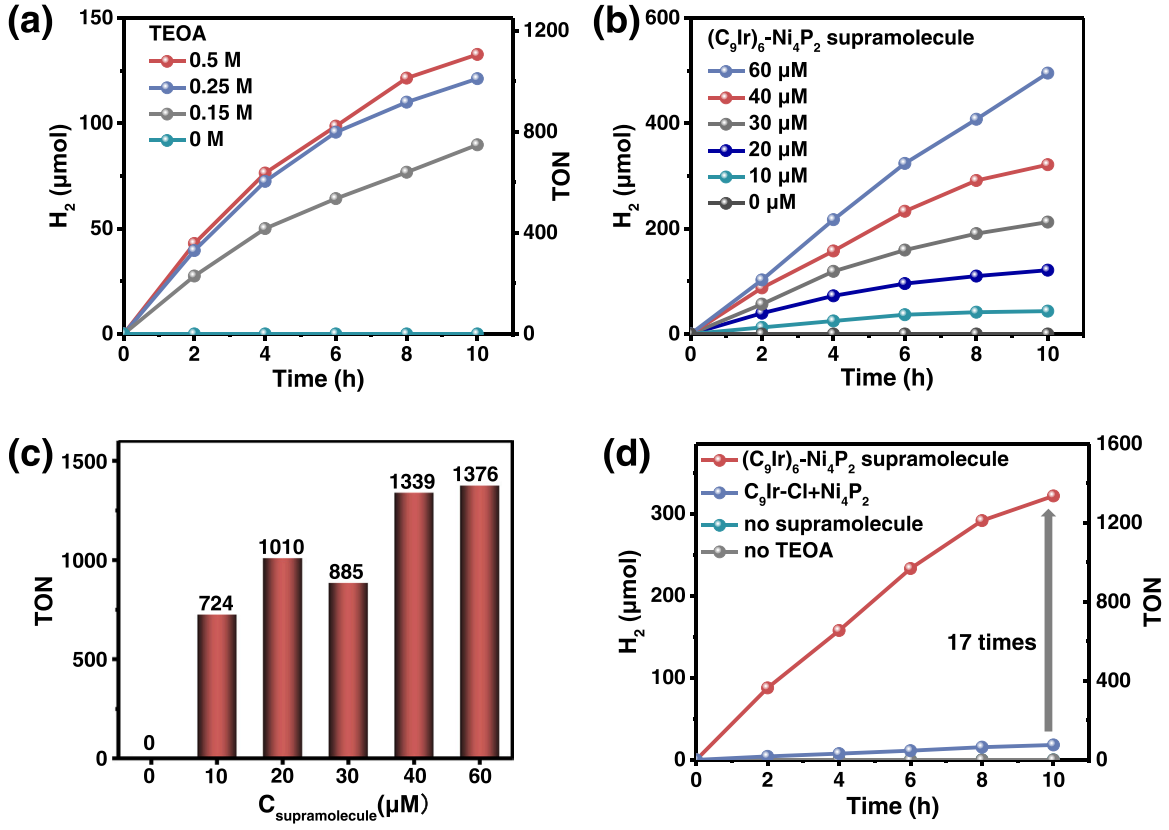

Fig. 3. Photocatalytic H_2 generation by varying concentration of (a) TEOA (0–0.5 M) with **$(C_9Ir)_6$-Ni_4P_2** supramolecule at 20 μM and (b) **$(C_9Ir)_6$-Ni_4P_2** supramolecule (0–60 μM) with TEOA at 0.25 M; (c) The TONs by tuning concentration of **$(C_9Ir)_6$-Ni_4P_2** supramolecule; (d) Control experiments of using identical **C_9Ir-Cl** (240 μM) and **Na_6K_4-Ni_4P_2** (40 μM) to replace **$(C_9Ir)_6$-Ni_4P_2** supramolecule (40 μM). Condition: Xe lamp (λ > 400 nm, 300 W, 25 ℃), H_2O (2 M), 6 mL DMF/toluene (v/v = 3/1), 10 h.

$(C_9Ir)_6$-Ni_4P_2 supramolecule from 10 μM to 60 μM also significantly accelerated the photocatalytic process (Fig. 3b), the calculated TONs of these systems increased from 724 to 1376 accordingly (Fig. 3c), corresponding to an apparent quantum yield (AQY) increase from 0.03% to 0.26% (Table S2). These results proved that delicately adjusting the amount of **$(C_9Ir)_6$-Ni_4P_2** supramolecule and TEOA could obviously influence the catalytic rate to achieve efficient hydrogen production.

To investigate the advantage of **$(C_9Ir)_6$-Ni_4P_2** supramolecule for efficient catalysis, a comparative experiment (Fig. 3d) has been conducted by replacing **$(C_9Ir)_6$-Ni_4P_2** supramolecule (40 μM) with equivalents molar concentration of discrete **C_9Ir-Cl** (240 μM) photosensitizer and **Na_6K_4-Ni_4P_2** (40 μM) catalyst. Under otherwise identical condition, the latter catalytic system gave rise to a TON of only 76 (~18 μmol H_2 gas) in 10 h, which is 16 times lower than that of **$(C_9Ir)_6$-Ni_4P_2** supramolecule-catalyzed system (TON ~1339). Such obvious difference clearly illustrated the superiority of integrating photosensitizer and catalyst into electrostatically assembled supramolecule, which, to some extent, outperforms the related literature reports (Table S3). The outperformance of **$(C_9Ir)_6$-Ni_4P_2** supramolecule could be ascribed to the improved ET processes via intramolecular routes, resulting in efficient quenching process between excited states of **C_9Ir** photosensitizers and **Ni_4P_2** catalysts. In other words, the closer distance and ordered arrangement of photosensitizer and catalyst in supramolecule could induce much more efficient charge transfer between those two important units, which is beneficial for photocatalytic hydrogen generation.

3.4. Stability test of $(C_9Ir)_6$-Ni_4P_2 supramolecule containing system

To verify the stability of photocatalytic system, a series of experiments were carried out. Firstly, we have evaluated the long-term catalytic activity of **$(C_9Ir)_6$-Ni_4P_2** supramolecule containing system (Fig. 4a). After 96 h irradiation, a TON of as high as 4004 (~961 μmol H_2 gas) was achieved, proving the robustness and high durability of the system in prolonging photocatalysis. As the **$(C_9Ir)_6$-Ni_4P_2** supramolecule is composed of cationic **C_9Ir** part and poly-anionic **Ni_4P_2** part, thus it could be easily isolated from photocatalytic solution by changing the polarity of the reaction solution with addition of excess amount of water. As shown in Fig. 4b, the FT-IR spectra of recovered **$(C_9Ir)_6$-Ni_4P_2** supramolecule displayed negligible changes before and after photocatalytic reaction for 10 h. The stability of **$(C_9Ir)_6$-Ni_4P_2** supramolecule was further confirmed by monitoring its UV–Vis absorption spectra change in DMF/toluene (v/v: 3/1) solvent under light and air condition for four days. As shown in Fig. 4c, the absorption intensity of **$(C_9Ir)_6$-Ni_4P_2** supramolecule solution displayed no decrease or shifts even for 96 h, the main absorption bands ranging from 250 nm to 350 nm (metal-perturbed intraligand transitions) and from 400 nm to 520 nm (ILCT of coumarin) remained largely unchanged. All those results demonstrated the high photostability of both **$(C_9Ir)_6$-Ni_4P_2** supramolecule and its photocatalytic system, which guaranteed a highly efficient and long-term stable hydrogen production.

3.5. The effect of solvent polarity and electrolyte

It's known that the electrostatic interaction induced assemblies could be easily controlled by adjusting the polarity of solvents [49]. Therefore, to elucidate the effect of solvent polarity, we have utilized mixtures of H_2O/DMF, 1,4-dioxane/DMF, ethyl acetate/DMF and ether/DMF in a ratio of 1/3 to replace photocatalytic solution of

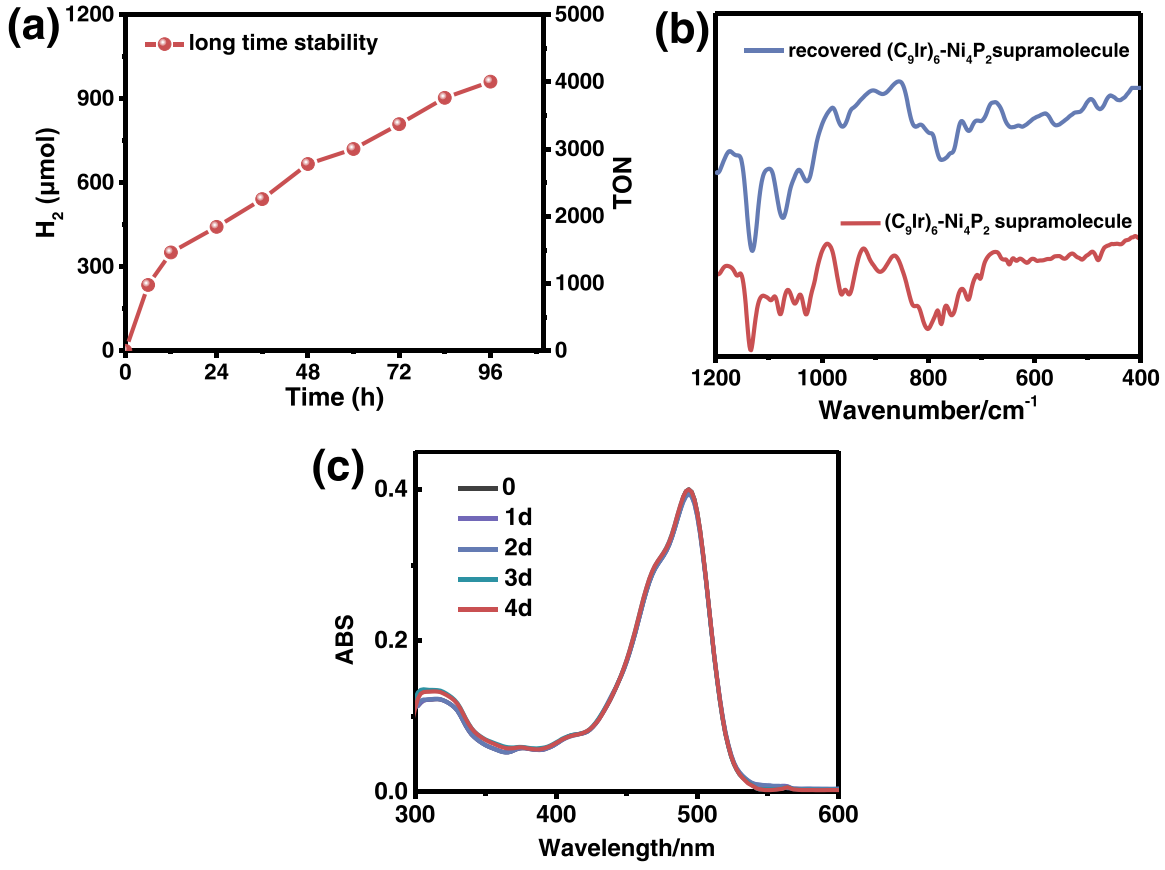

Fig. 4. (a) Long-term hydrogen evolution of **$(C_9Ir)_6$-Ni_4P_2** supramolecule containing system. Condition: Xe lamp (λ > 400 nm, 300 W, 25 ℃), **$(C_9Ir)_6$-Ni_4P_2** supramolecule (40 μM), TEOA (0.25 M), H_2O (2 M), 6 mL DMF/toluene (v/v = 3/1), 10 h; (b) FT-IR spectra of recovered **$(C_9Ir)_6$-Ni_4P_2** supramolecule by removing the reaction solvent before and after photocatalysis for 10 h, 2 wt% in KBr; (c) The stability of **$(C_9Ir)_6$-Ni_4P_2** supramolecule in DMF/toluene (v/v=3/1) by monitoring their UV-Vis spectra *versus* time.

toluene/DMF, respectively. The polarity value is in the order of 10.2 > 4.8 > 4.3 > 2.9 > 2.4 for that of H_2O, 1,4-dioxane, ethyl acetate, ether, and toluene, respectively. Under otherwise identical condition, the corresponding systems produced catalytic TONs of 38, 257, 1097, 1298, and 1339, respectively (Fig. 5a). The H_2 yield, TONs of H_2 generation, and the calculated AQY values increased significantly as the solvent polarity decreased (Fig. 5b, Table S2). It could be attributed to the fact that tuning the polarity of catalytic solvents from polar to non-polar trend could induce much closer and ordered assembly between positively-charged $\mathbf{C_9Ir^+}$ chromophore and negatively-charged $\mathbf{Ni_4P_2}$ catalyst in the obtained $\mathbf{(C_9Ir)_6\text{-}Ni_4P_2}$ supramolecule (Fig. 5c). Such closer distance and ordered arrangement between the two components could be beneficial for much more efficient photocatalytic process. To verify this explanation, an additional experiment by adding NaCl salts into photocatalytic solution (toluene/DMF) was further conducted. The presence of 6 equivalents of NaCl could largely destroy the ordered electrostatic interaction of $\mathbf{(C_9Ir)_6\text{-}Ni_4P_2}$ supramolecule, resulting in a distribution of the two components in chaos manner. Therefore, the yield of hydrogen production was remarkably decreased (Fig. 5d). Further increasing the concentration of added NaCl to 36 equivalents also produced a similar very low TON. These observations clearly proved the significance of such ordered supramolecular structure for effective photocatalysis.

3.6. Supramolecular conformation in solution

To more directly elucidate the conformations of $\mathbf{(C_9Ir)_6\text{-}Ni_4P_2}$ supramolecule in solution, transmission electron microscope (TEM) and dynamic light scattering (DLS) techniques were used to characterize a series of reaction solutions. The TEM images of ordered $\mathbf{(C_9Ir)_6\text{-}Ni_4P_2}$ supramolecule display a uniformly dispersed vesicle-like structure in photocatalytic DMF/toluene (3/1) solution (Fig. 6a and b) with a mean size distribution of ~2.8 nm (Fig. 6c), which is in good agreement with the average size distribution of 2.7 nm as obtained from the DLS measurement (Fig. S8). The observed hydrodynamic size distribution (~2.7 nm) is very close to the theoretically calculated size (~2.9 nm) by including one $\mathbf{Ni_4P_2}$ polyoxoanion (~1.3 nm) and two straightly lined $\mathbf{C_9Ir^+}$ cations (~0.8 nm) as shown in Fig. 1. Such ordered supramolecular structures contributed greatly to efficient photocatalytic hydrogen production as observed in above catalytic experiments (Fig. 3d and Fig. 5d). In comparison, no such ordered supramolecular architecture was observed for the solution of individual $\mathbf{Ni_4P_2}$ POM in DMF/toluene (3/1) solution in the absence of $\mathbf{C_9Ir^+}$ cations (Fig. 6d). The DLS measurement on such individual $\mathbf{Ni_4P_2}$ POM solution gives rise to a mean hydrodynamic size of ~1.0 nm (Fig. S9), which reflects the molecular size of discrete $\mathbf{Ni_4P_2}$ polyoxoanion (around 1.3 nm). In addition, no vesicle-like assembly has been observed while dissolving the $\mathbf{(C_9Ir)_6\text{-}Ni_4P_2}$ supramolecule into DMF/H_2O (3/1) solution (Fig. 6e), and in the meanwhile a hydrodynamic size distribution of ~1.1 nm has been detected by DLS measurement (Fig. S10), consistent with the discrete distribution of individual $\mathbf{Ni_4P_2}$ polyoxoanion. These results further confirm the vital role of solvent polarity in successful formation of $\mathbf{(C_9Ir)_6\text{-}Ni_4P_2}$ supramolecular structures. More importantly, addition of excess amount of NaCl electrolyte to the DMF/toluene (3/1) solution of $\mathbf{(C_9Ir)_6\text{-}Ni_4P_2}$ supramolecule can also lead to the destruction of ordered vesicle-like assemblies (Fig. 6f) as expected. Also, a mean hydrodynamic size distribution of ~1.4 nm has been detected (Fig. S11), which is very close to that of independent $\mathbf{Ni_4P_2}$ polyoxoanion. Such destroyed $\mathbf{(C_9Ir)_6\text{-}Ni_4P_2}$ supramolecular assembly resulted in a remarkable decrease of photocatalytic activity for hydrogen production (Fig. 5d). All above results proved the essential role of appropriate solvent polarity and electrolyte for the successful electrostatic formation of $\mathbf{(C_9Ir)_6\text{-}Ni_4P_2}$ supramolecular assembly, which further greatly affect the photocatalytic performance for hydrogen evolution.

3.7. Proposed photocatalytic mechanism

To confirm the electron transfer dynamics in photocatalytic process,

(a)

Polarity value	solvent	TON/10h (solvent/DMF=1/3 v/v)
10.2	H_2O	38
4.8	1,4-dioxane	257
4.3	ethyl acetate	1097
2.9	ether	1298
2.4	toluene	1339

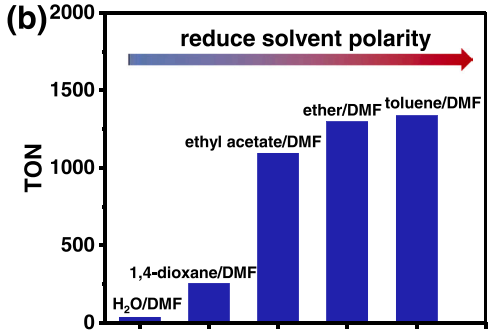

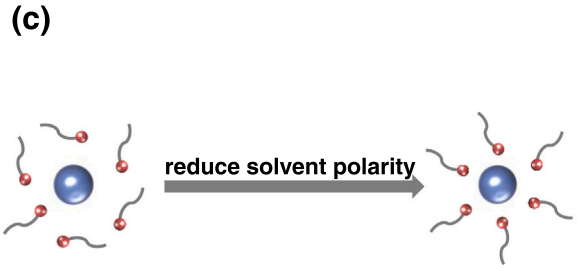

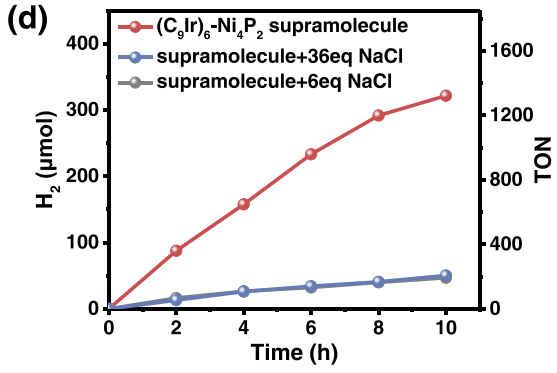

Fig. 5. (a) The polarity value of solvents and TONs of H_2 by using $\mathbf{(C_9Ir)_6\text{-}Ni_4P_2}$ supramolecule in corresponding solvents/DMF (v/v = 1/3); (b) The effect on hydrogen production by lowering polarity of solvents; (c) The illustration of structural variation of $\mathbf{(C_9Ir)_6\text{-}Ni_4P_2}$ supramolecule induced by solvents; (d) The influence of hydrogen generation with addition of NaCl electrolyte in system.

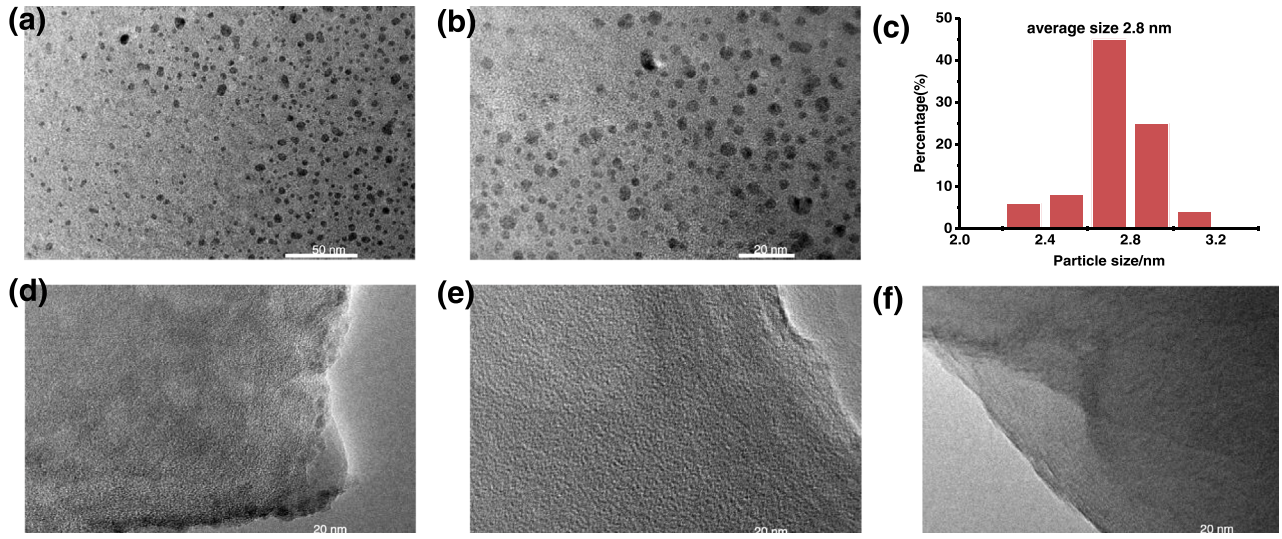

Fig. 6. Bright field TEM images of $(C_9Ir)_6$-Ni_4P_2 in DMF/Toluene (3/1) solution under scale bars of (a) 50 nm; (b) 20 nm, and (c) corresponding size distribution of $(C_9Ir)_6$-Ni_4P_2 in DMF/ Toluene (3/1) solution. TEM images of (d) Ni_4P_2 in DMF/ Toluene (3/1) solution, (e) $(C_9Ir)_6$-Ni_4P_2 in DMF/H_2O (3/1) solution and (f) adding NaCl electrolyte to $(C_9Ir)_6$-Ni_4P_2 in DMF/Toluene (3/1) solution.

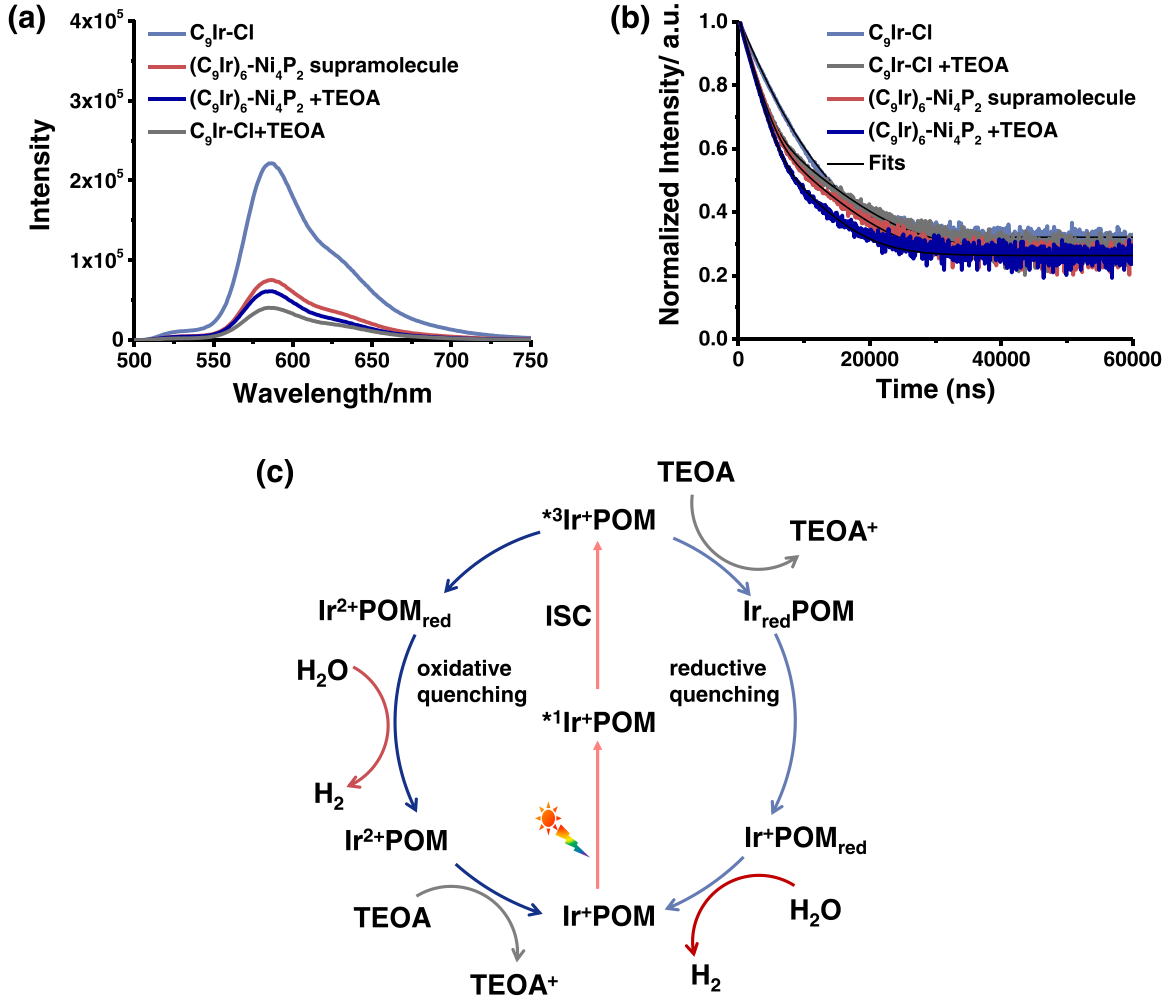

Fig. 7. (a) Emission and (b) decay kinetics of **C_9Ir-Cl** (240 μM), $(C_9Ir)_6$-Ni_4P_2 supramolecule (40 μM), C_9Ir-Cl (240 μM) quenched by TEOA (0.25 M) and $(C_9Ir)_6$-Ni_4P_2 supramolecule (40 μM) quenched by TEOA (0.25 M) in DMF/toluene (v/v = 3/1) solution under Ar condition (λ_{ex} = 400 nm, λ_{em} = 586 and BW 4, 4 for emission, λ_{em} = 586 nm for decay); (c) proposed photocatalytic mechanism.

luminescence tests were conducted in DMF/toluene (3/1) solution under Ar atmosphere by using steady-state and time-resolved fluorescence spectroscopy. As shown in Fig. 7a, the emission intensity of **C_9Ir-Cl** was significantly quenched after formation of **$(C_9Ir)_6$-Ni_4P_2** supramolecule, implying the efficient electron transfer between photoexcited states of **C_9Ir** photosensitizer and **Ni_4P_2** catalyst center. The emission intensity of **$(C_9Ir)_6$-Ni_4P_2** supramolecule further decreased by addition of TEOA (sacrificial reagent) under identical photocatalytic condition, indicating the existence of both oxidative and reductive quenching processes. In addition, the direct electron transfer between light-absorbing center and sacrificial reagent was further examined by adding TEOA to the solution of **C_9Ir-Cl**. It shows that the emission intensity of **C_9Ir-Cl** decreased dramatically upon addition of TEOA, proving the presence of reductive quenching process. With respect to the time-resolved luminescence decay data, all decay kinetics were analyzed by bi-exponential fitting. As shown in Fig. 7b, the formation of **$(C_9Ir)_6$-Ni_4P_2** supramolecule and presence of TEOA could obviously accelerate the quenching luminescence decay of **C_9Ir-Cl**, respectively. Besides, by adding TEOA into **$(C_9Ir)_6$-Ni_4P_2** supramolecule solution (Table S4), the lifetimes were quenched from 1.21 μs (τ_1) and 4.88 μs (τ_2) to 1.13 μs (τ_1) and 4.16 μs (τ_2), which is in good agreement with the results of above steady state spectroscopy experiments, proving the essential roles of both oxidative and reductive quenching processes for efficient photocatalytic H_2 evolution.

According to above luminescence studies, the proposed photocatalytic mechanism for H_2 production by utilizing **$(C_9Ir)_6$-Ni_4P_2** supramolecule is schematically displayed in Fig. 7c. Upon illumination, the **$(C_9Ir)_6$-Ni_4P_2** supramolecule (Ir^+POM) absorbed photos to produce singlet excited state ($^{*1}Ir^+$POM), which subsequently transfer to its triplet excited state ($^{*3}Ir^+$POM) through intersystem crossing process. The resulted $^{*3}Ir^+$POM could proceed either oxidative quenching pathway to produce $Ir^{2+}POM_{red}$ through charge separation or reductive quenching process to generate Ir_{red}POM by TEOA. The reduced state of POM in $Ir^{2+}POM_{red}$ species further catalyzed water to H_2 accompanying with the formation of Ir^{2+}POM, which could subsequently receive electron from TEOA and finally return to its initial state. In reductive quenching process, Ir_{red}POM proceeded charge separation to generate Ir^+POM_{red}, which further reduced H_2O to H_2 and returned to its ground state. The proposed mechanism revealed that the efficient electron transfer in integrated photosensitizer-catalyst structure of **$(C_9Ir)_6$-Ni_4P_2** supramolecule has greatly facilitated the photocatalytic hydrogen evolution.

4. Conclusion

In conclusion, a dual-functional **$(C_9Ir)_6$-Ni_4P_2** supramolecule has been successfully constructed via a facile cation-exchange approach to integrate the positively-charged **C_9Ir^+** chromophore and the negatively-charged **Ni_4P_2** polyoxoanion catalyst. The obtained **$(C_9Ir)_6$-Ni_4P_2** supramolecule has been systematically characterized by various spectroscopic techniques both in solid state and solution. Such dual-functional **$(C_9Ir)_6$-Ni_4P_2** supramolecule can work efficiently as both light-absorber and catalyst for hydrogen production under visible light irradiation. Under minimally optimized conditions, a catalytic TON of over 4000 (~961 μmol H_2 gas) was achieved after 96-hour photocatalysis, proving the robustness and high durability of the photocatalytic system. A series of experimental results (including TEM and DLS measurements as well as the effect of solvent polarity and electrolyte) strongly confirmed that the successful formation of **$(C_9Ir)_6$-Ni_4P_2** supramolecular vesicle-like assemblies in reaction solution is essential for efficient photocatalytic hydrogen production. Destruction of such ordered vesicle-like assemblies will lead to remarkable decrease of photocatalytic hydrogen production activity. Mechanistic studies further revealed the presence of both oxidative and reductive quenching processes during photocatalysis and also confirmed that the formation of **$(C_9Ir)_6$-Ni_4P_2** supramolecule is beneficial for effective electron transfer between **C_9Ir^+** chromophore and **Ni_4P_2** catalyst. This work provides new possibilities for the development of supramolecular photocatalytic hydrogen production systems, such facile cation-exchange approach could also be extended to construct other dual-functional photosensitizer-catalyst supramolecules for other interesting catalytic applications.

CRediT authorship contribution statement

Lin Qin: Data curation, Methodology, Writing – original draft, Investigation, Conceptualization. **Ruijie Wang:** Software, Validation. **Xing Xin**: Software, Visualization. **Mo Zhang:** Visualization, Resources. **Tianfu Liu:** Validation. **Hongjin Lv:** Funding acquisition, Project administration, Conceptualization, Supervision, Validation, Writing – review & editing. **Guo-Yu Yang:** Funding acquisition, Supervision.

Declaration of Competing Interest

The authors declare that they have no known competing financial interests or personal relationships that could have appeared to influence the work reported in this paper.

Acknowledgements

This work is supported by the National Natural Science Foundation of China (No. 21871025, No. 21831001 and No. 22101022), the Recruitment Program of Global Experts (Young Talents) and BIT Excellent Young Scholars Research Fund. The instrumental support from the Analysis and Testing Center of Beijing Instituted of Technology is also highly appreciated.

Appendix A. Supporting information

Supplementary data associated with this article can be found in the online version at doi:10.1016/j.apcatb.2022.121386.

References

[1] N. Kaeffer, M. Chavarot-Kerlidou, V. Artero, Hydrogen evolution catalyzed by cobalt diimine dioxime complexes, Acc. Chem. Res. 48 (2015) 1286–1295.
[2] M. Wang, K. Han, S. Zhang, L.C. Sun, Integration of organometallic complexes with semiconductors and other nanomaterials for photocatalytic H_2 production, Coord. Chem. Rev. 287 (2015) 1–14.
[3] A.J. Esswein, D.G. Nocera, Hydrogen production by molecular photocatalysis, Chem. Rev. 107 (2007) 4022–4047.
[4] H. Lv, Y.V. Geletii, C.C. Zhao, J.W. Vickers, G.B. Zhu, Z. Luo, J. Song, T.Q. Lian, D. G. Musaev, C.L. Hill, Polyoxometalate water oxidation catalysts and the production of green fuel, Chem. Soc. Rev. 41 (2012) 7572–7589.
[5] Z.J. Han, R. Eisenberg, Fuel from water: the photochemical generation of hydrogen from water, Acc. Chem. Res. 47 (2014) 2537–2544.
[6] Y.J. Yuan, Z.T. Yu, D.Q. Chen, Z.G. Zou, Metal-complex chromophores for solar hydrogen generation, Chem. Soc. Rev. 46 (2017) 603–631.
[7] X.B. Li, C.H. Tung, L.Z. Wu, Semiconducting quantum dots for artificial photosynthesis, Nat. Rev. Chem. 2 (2018) 160–173.
[8] Q.Q. Bi, J.W. Wang, J.X. Lv, J. Wang, W. Zhang, T.B. Lu, Selective photocatalytic CO_2 reduction in water by electrostatic assembly of CdS nanocrystals with a dinuclear cobalt catalyst, ACS Catal. 8 (2018) 11815–11821.
[9] P. Wang, S. Guo, H.J. Wang, K.K. Chen, N. Zhang, Z.M. Zhang, T.B. Lu, A broadband and strong visible-light-absorbing photosensitizer boosts hydrogen evolution, Nat. Commun. 10 (2019) 1–12.
[10] A.S. Weingarten, R.V. Kazantsev, L.C. Palmer, M. McClendon, A.R. Koltonow, A.P. S. Samuel, D.J. Kiebala, M.R. Wasielewski, S.I. Stupp, Self-assembling hydrogel scaffolds for photocatalytic hydrogen production, Nat. Chem. 6 (2014) 964–970.
[11] Y. Liu, Z.Y. Zhang, Y.R. Fang, B.K. Liu, J.D. Huang, F.J. Miao, Y.N. Bao, B. Dong, IR-Driven strong plasmonic-coupling on Ag nanorices/$W_{18}O_{49}$ nanowires heterostructures for photo/thermal synergistic enhancement of H_2 evolution from ammonia borane, Appl. Catal. B: Environ. 252 (2019) 164–173.
[12] X.D. Jing, N. Lu, J.D. Huang, P. Zhang, Z.Y. Zhang, One-step hydrothermal synthesis of S-defect-controlled $ZnIn_2S_4$ microflowers with improved kinetics process of charge-carriers for photocatalytic H_2 evolution, J. Energy Chem. 58 (2021) 397–407.
[13] N. Lu, X.D. Jing, J.M. Zhang, P. Zhang, Q. Qiao, Z.Y. Zhang, Photo-assisted self-assembly synthesis of all 2D-layered heterojunction photocatalysts with long-range spatial separation of charge-carriers toward photocatalytic redox reactions, Chem. Eng. J. 431 (2022), 134001.

[14] A. Fihri, V. Artero, M. Razavet, C. Baffert, W. Leibl, M. Fontecave, Cobaloxime-based photocatalytic devices for hydrogen production, Angew. Chem. Int. Ed. 47 (2008) 564–567.

[15] P. Lei, M. Hedlund, R. Lomoth, H. Rensmo, O. Johansson, L. Hammarström, The Role of Colloid Formation in the Photoinduced H_2 Production with a Ru^{II}-Pd^{II} Supramolecular Complex: A Study by GC, XPS, and TEM, J. Am. Chem. Soc. 130 (2008) 26–27.

[16] Z.T. Yu, Y.J. Yuan, X. Chen, J.G. Cai, Z.G. Zou, Energy transfer in a hybrid Ir(III) carbene-Pt(II) acetylide assembly for efficient hydrogen production, Chem. -Eur. J. 21 (2015) 10003–10007.

[17] H. Ozawa, M. Haga, K. Sakai, A photo-hydrogen-evolving molecular device driving visible-light-induced EDTA-reduction of water into molecular hydrogen, J. Am. Chem. Soc. 128 (2006) 4926–4927.

[18] C. Li, M. Wang, J. Pan, P. Zhang, R. Zhang, L. Sun, Photochemical hydrogen production catalyzed by polypyridyl ruthenium–cobaloxime heterobinuclear complexes with different bridges, J. Organomet. Chem. 694 (2009) 2814–2819.

[19] S. Jasimuddin, T. Yamada, K. Fukuju, J. Otsuki, K. Sakai, Photocatalytic hydrogen production from water in self-assembled supramolecular iridium-cobalt systems, Chem. Commun. 46 (2010) 8466–8468.

[20] P. Zhang, M. Wang, C. Li, X. Li, J. Dong, L. Sun, Photochemical H_2 with noble-metal-free molecular devices comprising a porphyrin photosensitizer and a cobaloxime catalyst, Chem. Commun. 46 (2010) 8806–8808.

[21] S.S. Wang, G.Y. Yang, Recent advances in polyoxometalate-catalyzed reactions, Chem. Rev. 115 (2015) 4893–4962.

[22] L. Cronin, A. Muller, From serendipity to design of polyoxometalates at the nanoscale, aesthetic beauty and applications, Chem. Soc. Rev. 41 (2012) 7333–7334.

[23] M. Zhang, H. Li, J. Zhang, H. Lv, G.-Y. Yang, Research advances of light-driven hydrogen evolution using polyoxometalate-based catalysts, Chin. J. Catal. 42 (2021) 855–871.

[24] H.-L. Li, M. Zhang, C. Lian, Z.-L. Lang, H. Lv, G.-Y. Yang, Ring-shaped polyoxometalate built by $\{Mn_4PW_9\}$ and PO_4 units for efficient visible-light-driven hydrogen evolution, CCS Chem. 2 (2020) 2095–2103.

[25] W.C. Chen, S.T. Wu, C. Qin, X.L. Wang, K.Z. Shao, Z.M. Su, E.B. Wang, An unprecedented $\{Cu^{II}_{14}Te^{IV}_{10}\}$ core incorporated in a 36-tungsto-4-silicate polyoxometalate with visible light-driven catalytic hydrogen evolution activity, Dalton Trans. 47 (2018) 16403–16407.

[26] H. Lv, J. Song, Y.V. Geletii, J.W. Vickers, J.M. Sumliner, D.G. Musaev, P. Kögerler, P.F. Zhuk, J. Bacsa, G. Zhu, C.L. Hill, An exceptionally fast homogeneous carbon-free cobalt-based water oxidation catalyst, J. Am. Chem. Soc. 136 (2014) 9268–9271.

[27] H. Lv, J. Song, Y.V. Geletii, W.W. Guo, J. Bacsa, C.L. Hill, A hexanuclear cobalt(II) cluster incorporated in a banana-shaped tungstovanadate: $[(Co(OH_2)Co_2VW_9O_{34})_2(VW_6O_{26})]^{17-}$, Eur. J. Inorg. Chem. (2013) 1720–1725.

[28] W. Guo, H. Lv, Z.Y. Chen, K.P. Sullivan, S.M. Lauinger, Y.N. Chi, J.M. Sumliner, T. Q. Lian, C.L. Hill, Self-assembly of polyoxometalates, Pt nanoparticles and metal-organic frameworks into a hybrid material for synergistic hydrogen evolution, J. Mater. Chem. A. 4 (2016) 5952–5957.

[29] W. Guo, H. Lv, J. Bacsa, Y. Gao, J.S. Lee, C.L. Hill, Syntheses, structural characterization, and catalytic properties of Di- and trinickel polyoxometalates, Inorg. Chem. 55 (2016) 461–466.

[30] J.M. Sumliner, H. Lv, J. Fielden, Y.V. Geletii, C.L. Hill, Polyoxometalate multi-electron-transfer catalytic systems for water splitting, Eur. J. Inorg. Chem. (2014) 635–644.

[31] J.W. Vickers, H. Lv, J.M. Sumliner, G. Zhu, Z. Luo, D.G. Musaev, Y.V. Geletii, C. L. Hill, Differentiating homogeneous and heterogeneous water oxidation catalysis: confirmation that $[Co_4(H_2O)_2(\alpha\text{-}PW_9O_{34})_2]^{10-}$ Is a molecular water oxidation catalyst, J. Am. Chem. Soc. 135 (2013) 14110–14118.

[32] H. Lv, W. Guo, K.F. Wu, Z.Y. Chen, J. Bacsa, D.G. Musaev, Y.V. Geletii, S. M. Lauinger, T. Lian, C.L. Hill, A noble-metal-free, tetra-nickel polyoxotungstate catalyst for efficient photocatalytic hydrogen evolution, J. Am. Chem. Soc. 136 (2014) 14015–14018.

[33] H. Lv, J. Song, H.M. Zhu, Y.V. Geletii, J. Bacsa, C.C. Zhao, T.Q. Lian, D.G. Musaev, C.L. Hill, Visible-light-driven hydrogen evolution from water using a noble-metal-free polyoxometalate catalyst, J. Catal. 307 (2013) 48–54.

[34] H. Lv, Y.N. Chi, J. van Leusen, P. Kogerler, Z.Y. Chen, J. Bacsa, Y.V. Geletii, W. Guo, T.Q. Lian, C.L. Hill, $[\{Ni_4(OH)_3AsO_4\}_4(B\text{-}\alpha\text{-}PW_9O_{34})_4]^{28-}$: a new polyoxometalate structural family with catalytic hydrogen evolution activity, Chem. -Eur. J. 21 (2015) 17363–17370.

[35] H. Lv, Y.Z. Gao, W. Guo, S.M. Lauinger, Y.N. Chi, J. Bacsa, K.P. Sullivan, M. Wieliczko, D.G. Musaev, C.L. Hill, Cu-based POlyoxometalate Catalyst for Efficient Catalytic Hydrogen Evolution, Inorg. Chem. 55 (2016) 6750–6758.

[36] T.T. Cui, L. Qin, F.Y. Fu, X. Xin, H.J. Li, X.K. Fang, H. Lv, Pentadecanuclear Fe-containing polyoxometalate catalyst for visible-light-driven generation of hydrogen, Inorg. Chem. 60 (2021) 4124–4132.

[37] H. Li, L. Qin, L.-Y. Yao, H. Lv, Syntheses and catalytic properties of two new multi-manganese-substituted silicotungstates, J. Coord. Chem. 73 (2020) 2410–2421.

[38] L. Jiao, Y. Dong, X. Xin, L. Qin, H. Lv, Facile integration of Ni-substituted polyoxometalate catalysts into mesoporous light-responsive metal-organic framework for effective photogeneration of hydrogen, Appl. Catal. B Environ. 291 (2021) 120091–120101.

[39] L. Qin, C. Zhao, L.-Y. Yao, H. Dou, M. Zhang, J. Xie, T.-C. Weng, H. Lv, G.-Y. Yang, Efficient photogeneration of hydrogen boosted by long-lived dye-modified Ir(III) photosensitizers and polyoxometalate catalyst, CCS Chem. 3 (2021) 651–663.

[40] W.L. Sun, C. He, T. Liu, C.Y. Duan, Synergistic catalysis for light-driven proton reduction using a polyoxometalate-based Cu-Ni heterometallic-organic framework, Chem. Commun. 55 (2019) 3805–3808.

[41] D.Y. Shi, R. Zheng, C.-S. Liu, D.-M. Chen, J. Zhao, M. Du, Dual-functionalized mixed keggin- and lindqvist-type Cu_{24}-based POM@MOF for visible-light-driven H_2 and O_2 evolution, Inorg. Chem. 58 (2019) 7229–7235.

[42] F.A. Black, A. Jacquart, G. Toupalas, S. Alves, A. Proust, I.P. Clark, E.A. Gibson, G. Izzet, Rapid photoinduced charge injection into covalent polyoxometalate-bodipy conjugates, Chem. Sci. 9 (2018) 5578–5584.

[43] S. Schönweiz, S.A. Rommel, J. Kübel, M. Micheel, B. Dietzek, S. Rau, C. Streb, Covalent photosensitizer-polyoxometalate-catalyst dyads for visible-light-driven hydrogen, Evol. Chem. Eur. J. 22 (2016) 12002–12005.

[44] S. Amthor, S. Knoll, M. Heiland, L. Zedler, C. Li, D. Nauroozi, W. Tobaschus, A. K. Mengele, M. Anjass, U.S. Schubert, B. Dietzek-Ivanšić, S. Rau, C. Streb, A photosensitizer–polyoxometalate dyad that enables the decoupling of light and dark reactions for delayed on-demand solar hydrogen production, Nat. Chem. 14 (2022) 321–327.

[45] A. Proust, B. Matt, R. Villanneau, G. Guillemot, P. Gouzerha, G. Izzet, Functionalization and post-functionalization: a step towards polyoxometalate-based materials, Chem. Soc. Rev. 41 (2012) 7605–7622.

[46] B. Matt, J. Fize, J. Moussa, H. Amouri, A. Pereira, V. Artero, G. Izzet, A. Proust, Charge photo-accumulation and photocatalytic hydrogen evolution under visible light at an iridium(III)-photosensitized polyoxotungstate, Energ. Environ. Sci. 6 (2013) 1504–1508.

[47] B. Matt, X. Xiang, A.L. Kaledin, N. Han, J. Moussa, H. Amouri, S. Alves, C.L. Hill, T. Lian, D.G. Musaev, G. Izzet, A. Proust, Long lived charge separation in iridium (III)- photosensitized polyoxometalates: synthesis, photophysical and computational studies of organometallic–redox tunable oxide assemblies, Chem. Sci. 4 (2013) 1737–1745.

[48] A. Misra, K. Kozma, C. Streb, M. Nyman, Beyond charge balance: counter-cations in polyoxometalate chemistry, Angew. Chem. Int. Ed. 59 (2020) 596–612.

[49] B. Li, W. Li, H. Li, L. Wu, Ionic complexes of metal oxide clusters for versatile self-assemblies, Acc. Chem. Res. 50 (2017) 1391–1399.

[50] H. Cruz, A.L. Pinto, J.C. Lima, L.C. Branco, S. Gago, Application of polyoxometalate-ionic liquids (POM-ILs) in dye-sensitized solar cells (DSSCs), Mater. Lett. 6 (2020) 100033–100038.

[51] J. Xie, B.F. Abrahams, A.G. Wedd, Facile assembly of hybrid materials containing polyoxometalate cluster anions and organic dye cations: crystal structures and initial spectral characterization, Chem. Commun. (2008) 576–578.

[52] H. Li, H. Sun, W. Qi, M. Xu, L. Wu, Onionlike hybrid assemblies based on surfactant-encapsulated polyoxometalates, Angew. Chem. Int. Ed. 46 (2007) 1300–1303.

[53] M. Nyman, M.A. Rodriguez, T.M. Anderson, D. Ingersoll, Two structures toward understanding evolution from surfactant-polyoxometalate lamellae to surfactant-encapsulated polyoxometalates, Cryst. Growth Des. 9 (2009) 3590–3597.

[54] I. Yoon, J.H. Kim, J.Z. Li, W.K. Lee, Y.K. Shim, Efficient photosensitization by a chlorin-polyoxometalate supramolecular complex, Inorg. Chem. 53 (2014) 3–5.

[55] M. Orlandi, R. Argazzi, A. Sartorel, M. Carraro, G. Scorrano, M. Bonchio, F. Scandola, Ruthenium polyoxometalate water splitting catalyst: very fast hole scavenging from photogenerated oxidants, Chem. Commun. 46 (2010) 3152–3154.

[56] J. Fielden, J.M. Sumliner, N. Han, Y.V. Geletii, X. Xiang, D.G. Musaev, T. Lian, C. L. Hill, Water splitting with polyoxometalate-treated photoanodes: enhancing performance through sensitizer design, Chem. Sci. 6 (2015) 5531–5543.

[57] X. Chen, G. Zhang, B. Li, L. Wu, An integrated giant polyoxometalate complex for photothermally enhanced catalytic oxidation, Sci. Adv. 7 (2021) eabf8413.

[58] M. Melchionna, P. Fornasiero, Updates on the roadmap for photocatalysis, ACS Catal. 10 (2020) 5493–5501.

[59] S. Cao, L. Piao, Considerations for a more accurate evaluation method for photocatalytic water splitting, Angew. Chem. Int. Ed. 59 (2020) 18312–18320.

[60] J.J. Walsh, D.L. Long, L. Cronin, A.M. Bond, R.J. Forstera, T.E. Keyes, Electronic and photophysical properties of adducts of $[Ru(bpy)_3]^{2+}$ and Dawson-type sulfite polyoxomolybdates $\alpha/\beta\text{-}[Mo_{18}O_{54}(SO_3)_2]^{4-}$, Dalton Trans. 40 (2011) 2038–2045.